This is a non-peer reviewed preprint submitted to EarthArXiv

It is currently under consideration at *Rock Mechanics and Rock Engineering*

Effect of Pressure and Stress cycles on fluid flow in hydraulically-fractured, low-porosity, anisotropic sandstone

Peter Ibemesi and Philip Benson

Rock Mechanics Laboratory, University of Portsmouth, Portsmouth, PO1 3QL, UK.

Corresponding author: Peter Ibemesi, Rock Mechanics Laboratory, School of Geography Environment and Geosciences, University of Portsmouth, Portsmouth, PO1 3QL, UK. (peter.ibemesi@port.ac.uk)

Abstract

Hydraulic fracture in deep rock masses is used across a variety of disciplines, from unconventional oil and gas to geothermal exploration. The overall efficiency of this process requires not only knowledge of the fracture mechanics of the rocks, but also how the newly generated fractures influence macro-scale pore connectivity. We here use cylindrical samples of Crab Orchard sandstone (90mm length and 36mm diameter), drilled with a central conduit of 9.6mm diameter, to simulate hydraulic fracture. Results show that the anisotropy (mm-scale cross-bedding orientation) affects breakdown pressure, and subsequent fluid flow. In experiments with samples cored parallel to bedding, breakdown pressures of 11.3MPa, 27.7MPa and 40.5MPa are recorded at initial confining pressures at injection of 5MPa, 11MPa and 16MPa respectively. An increase in confining pressure (from 5 MPa to 26 MPa) after the initial fracture event results in a flow rate decrease from 1.67 mL/min to 0.043 mL/min. For samples cored perpendicular to bedding, breakdown pressure of 15.4MPa, 27.4MPa and 34.2MPa were recorded at initial confining pressure at injection of 5MPa, 11MPa and 16MPa respectively. As confining pressure increases from 5 MPa to 26 MPa, flow rate through the newly generated fracture decreases from 0.043 mL/min to 0.0073 mL/min. We note that fluid flow recovers during a confining pressure "re-set" and that the ability of flow to recover is strongly dependent on sample anisotropy and initial confining pressure at injection.

Keywords: flow rate; confining pressure; tensile fracturing; acoustic emissions; anisotropy; tight sandstone;

List of symbols

P_b	Breakdown pressure
S_h	Minor horizontal stress
S_H	Major horizontal stress
σ_T	Tensile strength
P_0	Pore pressure
α	Biot poroelastic coefficient
v	Poisson's ratio
σ_{ax}	Axial pressure
k_w	Wall permeability
k_{wc}	Critical wall permeability

Declarations

Conflict of Interest

The authors declare no conflict of interest.

Acknowledgments

The authors acknowledge Emily Butcher for technical support in the Rock Mechanics Laboratory, and Smart Osarenogowu for thoughtful discussions. This research was funded by a Petroleum Technology Development Fund (PTDF, Nigeria) to Peter Ibemesi and Philip Benson. This work was supported by the National Research Facility for Lab X-ray CT (NXCT) through EPSRC grant EP/T02593X/1.

Author Contributions

Peter Ibemesi wrote the manuscript and performed the experiments. Philip Benson designed the experiments, and supervised data curation and analysis.

Introduction

Hydraulic fracturing is an important natural phenomenon in the earth subsurface, exhibited across a range of processes including magma intrusion (Rubin 1993; Tuffen and Dingwell, 2005) and mineral emplacement (Richards, 2003). In the engineered environment, hydraulic fracturing has been used in the petroleum industry since the mid-1950's (Tuefel, 1981) to enhance oil and gas production from tight reservoirs (characterized by low permeability, often in the microDary range of 10-100's x 10^{-18} m^2). To date, hydraulic fracture has become a common, albeit controversial, practice to improve oil and gas recovery (Gillard et al., 2010; Kennedy et al., 2012; Wang et al., 2014). These new technologies have led some nations (for example the USA) to become significant producers of natural gas (Wang et al., 2014) as previously low permeable formations were fractured. However, the process is not without controversy, and additionally has been developed over years in a somewhat ‘ad-hoc’ or trial-and-error manner. This has resulted in varying degrees of overall success due to the complexities of reservoirs that contain significant structural, sedimentological and mechanical heterogeneities. Together, these features alter the relationship between the tensile fracture mechanics needed to generate new fractures for fluid movement, as balanced against the fundamental rock physical properties and local stress field (Martin and Chandler 1993; Sone, 2013; Gehne & Benson 2017; 2019).

The objective of hydraulic fracture is to increase the rock permeability through induced fracture in the rock mass. This is usually achieved by pumping a pore fluid (with or without additional propping agents to keep new fractures mechanically open) into a wellbore at a sufficiently high pressure to fracture the surrounding rock mass in tension. This requires a sufficiently high fluid flow rate to overcome the background permeability and radial fluid flow, which is a function of the permeability of the unfractured rock mass (Fazio et al., 2020). If the fluid injection is higher that the natural fluid dispersion rate, pressure builds up inside the borehole which leads to fracture, including reopening and further propagation of existing fractures when the *in-situ* tensile rock strength is exceeded. The resultant hydraulic fracture extends until the formation loss is greater than the pumping rate (Reinicke et al., 2010).

Different approaches have been applied to study the pressure (P_b) at which the rock first yields (fractures), known as the breakdown pressure. The simple linear elastic approach considers a defect-free, impermeable and non-porous rock matrix around the borehole (Hubbert and Willis, 1972; Jaeger et al., 2009) via

$$P_b = 3S_h - S_H + \boldsymbol{\sigma}_T \qquad [\text{Eq. }1]$$

where σ_T is the tensile strength (an inherent property of the rock), and S_h and S_H are the minimum and maximum horizontal stresses respectively.

However, the above approach represents an 'end-member' case as no rock is truly impermeable: all rocks contain pores and fractures, and when saturated with pore fluid exerting a fluid pressure P_0, [Eq. 1] above is modified to:

$$P_b = 3S_h - S_H + \boldsymbol{\sigma}_T - P_{\mathbf{0}} \qquad [\text{Eq. }2]$$

The expression above [Eq. 2] may be further modified by adding poroelastic effects which account for the rock being both porous and permeable (e.g. Haimson and Fairhurst, 1969; Jaeger et al., 2009):

$$P_b = \frac{3S_h - S_H + \sigma_T}{2 - \alpha \frac{1-2v}{1-v}} - P_0 \qquad [\text{Eq. }3]$$

where (α) is the Biot poroelastic coefficient and v is the Poisson's ratio.

A final, minor, modification considers the role of rock matrix permeability in hydraulic fracturing. In Fazio et al., 2020, [Eq. 3] is assumed to be only valid under conditions whereby the bulk rock permeability (k_w) at the interface between the injection fluids and the wall is below a critical permeability (k_{wc}). Adding these boundary conditions yields:

$$P_b = \frac{3S_h - S_H + \sigma_T}{2 - \alpha \frac{1-2v}{1-v}} - P_0 \qquad for\ k_w < k_{wc} \qquad [\mathrm{Eq.\,4}]$$

An accurate charaterisation of the fluid flow through the bulk rock mass is key to understanding reservoir properties (Tan et al., 2018). However, measuring permeability remains challenging due to its sensitivity to heterogeneity. This is further complicated by the strong anisotropy found in typical formations used for unconventional hydrocarbons (such as mudrock, shale and crossbedded/tight sandstone). Nonetheless, numerous studies using wellbore tools and core plugs have attempted to link the fracture process to permeability enhancement via numerical models (Ma et al., 2016). To calibrate these models and in-situ data, laboratory measurements of flow through fractures under controlled conditions have used images of the post-test fracture aperture (e.g. Stanchits, 2014) or morphology of the post-test shear fracture planes (Kranz et al., 1979; Bernier et al., 2004; Gillard et al., 2010, Zhang 2015), as a function of flow rate or permeability. Collectively, these experiments have provided useful data on fracture behavior, but have tended to focus on mudrocks (shale) over other rock types.

Here we report a new laboratory study designed to measure the fluid-flow rate through tensile fractures in a tight anisotropic sandstone (Crab Orchard), with respect to anisotropy. Fractures are freshly generated in the tensile mode using water, via the method of Gehne and Benson (2019) before fluid-flow data are taken, up to simulated reservoir conditions to 2.5km. Fracture aperture data are then imaged post-test using X-ray Computed Tomography (CT) to analyze the final fracture aperture to measured flow rate. Our laboratory set-up is designed to eliminate the possibility of altering the fracture properties when extracting the fractured sample as flow rate data is taken immediately after fracture, and so allows better comparison between the fluid-driven tensile fracture processes (and the associated flow enhancement), to reservoir conditions. Finally, we link these fracture mechanics and fluid flow through the fracture to the accompanying Acoustic Emission (AE, the laboratory proxy to tectonic seismicity) as an additional guide to the timing and development of fracture properties with respect to the mm-scale crossbedding.

Experimental methods

Sample Material and preparation

Crab Orchard sandstone (COS) has a relatively low permeability and porosity for a sandstone of approximately 10^{-18} m^2 and 5% respectively (Benson et al., 2003). The rock, from the Cumberland Plateau, Tennessee (USA), is a fine grained cross bedded fluvial sandstone, with sub-hedral to sub-rounded grains of about 0.25mm size. It consists predominantly of quartz (>80%) with little feldspar and lithic fragments cemented by sericitic clay (Benson et al., 2006). This material exhibits a high anisotropy (up to 20% P-wave velocity anisotropy and up to 100% permeability anisotropy), and has a tensile strength calculated through the Brazilian Disc (Ulusay, 2014) of 9.8 MPa perpendicular to bedding and 8.6 MPa parallel to bedding.

Cylindrical samples of 36mm diameter and approximately 90 mm in length were cored from blocks with a long axis either parallel (defined as the x-orientation) or normal (z-orientation) to the visible bedding plane (figure 1). Samples were then water-saturated by immersing under water using a vacuum pump to extract void space air for a minimum of 24 hours (for ‘saturated’ hydraulic fracture experiments). Each core sample had a central axially-drilled conduit of 10.5mm diameter through the length of the sample, generating a ‘thick-walled’ cylinder (figure 1A) arrangement that can be accommodated into a standard triaxial apparatus. The samples are inserted into a 3D printed liner (figure 1C) that is, in turn, is encapsulated in a rubber jacked (figure 1B). This allows water from generated tensile fractures to be received, regardless of their radial orientation, by a water outlet port (Gehne and Benson, 2019).

The sample setup is completed by fitting two steel waterguides (figure 1D) into the central conduit. These waterguides direct pressurized fluid into a sealed section of the drilled conduit (using O-rings), allowing fluid to apply a uniform pressure to the inner surface of the sealed section, leading to tensile fracture in the central section from which water flow is received via the outlet port, measured using a voluometer.

FIGURE 1

Hydraulic fracture procedure and protocol

Sample assemblies were mounted within a conventional servo-controlled triaxial machine capable of confining pressures up to 100 MPa (Figure 2). Four 100 MPa servo-controlled pumps provide: (i), axial pressure through a piston-mounted pressure intensifier to provide a maximum of 680 MPa axial stress, (ii), confining pressure up to 100 MPa. Both these pumps use heat transfer oil (Julabo Thermal HS) as pressurizing medium. Two pore pumps independently provide fluid pressure to (iii), the bottom of the sample (via the lower water-guide) and (iv), receive water through the generated tensile fracture and exiting via the fluid outlet. Pumps (iii) and (iv) are set to maintain a set pressure gradient and thus establish steady fluid flow through the freshly generated tensile fracture. The final flow rate value is only taken when the flow between the two pumps have achieved a steady, but equal and opposite rate to signify no leaks in the system and to allow transients to settle (approximately 2 minutes).

Mechanical data (stress, strain, fluid pressures) is recorded at both a 'low' recording rate of 1 sample/second and high sampling rates (10k samples/s), for axial strain and fluid injection pressure only, to record fast changing transients (Gehne et al., 2019). In addition, a suite of 11 acoustic emission sensors, fitted to ports in the engineered rubber jacket (Fig. 1B), received Acoustic Emission (AE) data to monitor fracture speed and progress. The AE signals are first amplified by 60 dB and then received on an ASC "Richter" AE recorder at 10 MHz. For accurate seismo-mechanical data synchronisation during the dynamic tensile fracture, the fluid injection pressure output is split across both mechanical and a single channel of the AE data acquisition systems through an amplified circuit as described by Gehne (2018). This allows data synchronization with an accuracy of ±0.01ms.

FIGURE 2

The experimental procedure spans three stages (Figure 3). Firstly, hydrostatic pressure is established by increasing the confining pressure and the axial pressure concomitantly to attain the target pressure, and a pre-fracture measurement of fluid flow is taken by setting a differential pressure of 2 MPa between central conduit and the fluid outlet port. Secondly, pore fluid injection was activated at a constant flow rate of 5mL/min resulting in an increasing conduit pressure, until failure (hydraulic fracture) occurred (Figure 3). Evidence of fracture development includes a sharp decrease in injection (pore) pressure, accompanied by a swarm of AE. Thirdly, after tensile failure, a fluid pressure gradient (differential fluid pressure of 2 MPa) was re-established between the conduit pressure and the fluid outlet port to initiate a steady state flow through the freshly generated tensile fracture(s). The volume of the two pressure pumps were monitored independently; steady state flow is reached when the volume change with time is equal and opposite for the two pumps, averaged across a 4-minute time period and after an initial 2 minutes elapsed to allow transient effects to decay away. This procedure was repeated as a function of confining pressure increase (and decrease) to investigate the effect of confining pressure and pressure hysteresis on flow rate.

FIGURE 3

Results

Six experiments were conducted on COS at initial confining pressures (before injection) of 5 MPa, 11 MPa, and 16 MPa. At each pressure, a pair of samples were cored with long axis either parallel or perpendicular to bedding. As detailed above, for each sample an initial fluid flow is measured by setting a differential pore pressure (difference between conduit and outlet pressure) and measuring at the upstream and downstream reservoir (Fig. 3). These initial flow rate data are tabulated in Table 1.

TABLE 1

Hydraulic fracture

The hydraulic fracture stage of the experiment is initiated by injecting water into the sample at a fixed flow rate of 5mL/min. Data from sample COSx-1 (5 MPa initial confining pressure, core axis parallel to bedding) is shown in figure 4. As fluid was injected, a concomitant increase in injection pressure is recorded. This continues until an experiment time of approximately 1276s where tensile fracture is recorded at an injection pressure (or breakdown pressure, P_b) of

11.29 MPa, accompanied by a swarm of AE which increases steadily from 1260s, reaching a peak of 225 counts/s. After fracture, the injection pressure rapidly decreases to 2 MPa, and cumulative AE reaches a steady value.

FIGURE 4

At 5 MPa confining pressure but with the sample axis perpendicular to bedding (sample COSz-1), we see the injection pressure building until a breakdown pressure of 15.4 MPa (figure 5), some 4 MPa higher than sample COSx-1. Again, after the hydro-fracture event injection pressure decreases rapidly to approximately 2 MPa (figure 5). Relatively few AE events (and rather sparsely distributed in time) were recorded during the time of fluid injection (2344s to 2366s), however a swarm of activity was recorded at the moment of fracture. The cumulative AE counts increases rapidly at this point up to a peak of $4x10^4$ counts at 2367s.

FIGURE 5

At 11 MPa and parallel to bedding (experiment COSx-2), breakdown occurs at an injection pressure of 27.7 MPa (figure 6). Compared to COSx1, the injection fluid pressure dropped abruptly to approximately 5 MPa and it is again accompanied with a swarm of AE at 2364s (figure 6). The cumulative AE steadily increases from 4598s to $2\ x10^2$ counts after approximately 4630s, followed by a significant and rapid final increase at the moment of fracture at 4634s and a peak of 10^5 counts.

FIGURE 6

Mechanical data for sample COSz-2 (11 MPa and perpendicular to bedding) is shown in figure 7. Data exhibits a similar trend in injection pressure as previously seen for sample COSz-1, with a sharp decrease as tensile fracture is generated accompanied by a peak in AE events. However, a breakdown in injection pressure of 27.3 MPa is recorded in COSz-2, which decreases rapidly to approximately 6 MPa, again accompanied by a swarm of AE events which decrease in counts over time until approximately 3540s. However, the trend of AE leading up to failure is different, with no build-up in AE prior to the prominent swarm of activity failure time, resulting in a large cumulative AE count of 1.2 $x10^6$ counts at 3531s (sample failure).

FIGURE 7

At 16 MPa and parallel to bedding (experiment COSx-3), breakdown occurs at an injection pressure of 40.4 MPa which decreases rapidly to approximately 15 MPa after fracture, again accompanied with a swarm of AE (figure 8). Abundant AEs were recorded from approximately 4955s, rapidly increasing at the moment of breakdown pressure when compared with samples COSx-1 and COSx-2 (fig.8). Cumulative AE count increases at 4956s to a peak of 7x 10^5 at 4981s.

FIGURE 8

Finally, for sample COSz-3 (16 MPa and parallel to bedding), tensile fracture was recorded at injection pressure of 33.9 MPa accompanied once again by a swarm of AE (figure 9). Notably, the conduit pressure decreased slowly after fracture, only reaching 15.25 MPa after 30s had elapsed. Similarly to previous experiments, abundant AEs were recorded with an increase in cumulative AE count first registered at 6919s, but this time with a second significant increase at 6940s to a peak of 2 x10^4 counts (figure 9).

FIGURE 9

Post-Fracture fluid flow

With the tensile (radial) fracture established across samples at three different initial confining pressures, and across two different orientations with respect to anisotropy, a set of fluid flow measurements are made. Fluid flow is measured in cycles of increasing confining pressure, followed by a 're-set' to the original confining pressure, followed by a second cycle of increasing confining pressure. Figure 10 shows data from COSx-1 and COSz-1 (5 MPa initial conditions). Here, an increase in confining pressure (from 5 MPa to 26 MPa) for COSx-1 results in flow rate decreasing from 1.67 mL/min to 0.043 mL/min respectively. During the re-set of confining pressure from 26 MPa to 5 MPa, flow rate recovered only marginally, increasing from 0.043 mL/min to 0.134 mL/min. The second cycle of confining pressure increase gives a further reduction of flow rate from 0.134 mL/min to 0.028 mL/min, lower than the minimum of the first cycle. Sample COSz-1 shows a decreasing flow rate from 0.6 mL/min at 5 MPa confining pressure to 0.027 mL/min at 26 MPa confining pressure. During the 're-set' of confining pressure from 26 MPa, flow rate recovered from 0.027 mL/min to 0.099

mL/min. The second cycle of confining pressure increase resulted to a further reduction in flow rate from 0.099 mL/min to 0.014 mL/min.

FIGURE 10

For sample COSx-2 (11 MPa initial conditions), a general decreasing trend in flow rate was measured for a confining pressure increase from 11 MPa to 31 MPa (Figure 11). In the first cycle, the flow rate decreases from 0.043 mL/min to 0.0073 mL/min respectively. The confining pressure re-set resulted in a flow rate recovery from 0.0073 mL/min to 0.014 mL/min. The second cycle of confining pressure increase generates a reduction in flow rate from 0.014 mL/min to 0.0067 mL/min. Conversely, for COSz-2, the flow rate decreases from 0.0375 mL/min to 0.0042 mL/min at between 11 and 31 MPa confining pressure respectively. Pressure is again re-set, resulting in a flow rate recovery from 0.0042 mL/min to 0.0105 mL/min. The second cycle of confining pressure increase gives a further reduction of flow rate from 0.0105 mL/min to 0.0013 mL/min.

FIGURE 11

For sample COSx-3 (16 MPa initial conditions), flow rate decreases from 0.27 mL/min to 0.05 mL/min from 16 MPa to 31MPa respectively (figure 12). Confining pressure re-set results in a marginal flow rate recovery from 0.05 mL/min to 0.09 mL/min. The second cycle of confining pressure increase then results in a further decrease in the flow rate from 0.09 mL/min to 0.029 mL/min. Conversely, for sample COSz-3 (figure 12) flow decreases from 0.09 mL/min at 16 MPa confining pressure to 0.017 mL/min at 31 MPa. Confining pressure is again ‘re-set’ from

31 MPa to 16 MPa resulting in almost no recovery (0.017 to 0.018 mL/min) followed by a final confining pressure increase which resulted to a further decrease in the flow rate from 0.018 mL/min to 0.011 mL/min.

FIGURE 12

Discussion

Hydraulic fracturing has been established as a key process in both a natural environment (e.g. magma intrusion, and mineralization) as well as the engineered geo-environment, most frequently to develop hydraulic fractures in unconventional reservoirs (Guo et al., 2013; Gehne and Benson, 2017; Tan et al., 2018; Gehne and Benson, 2019). The ultimate aim of these methods is to generate conduits for fluid flow through tensile fracture and damage zone. However, whilst there have been a large number of studies investigating the fluid flow and permeability properties of highly anisotropic rocks such as shale (e.g.; Walsh, 1981; Benson et al., 2005; Gehne & Benson, 2017), and studies investigating the fracture mechanics (e.g. Hubbert and Willis, 1972; Zoback et al., 1977; Teufel and Clark, 1981; Rubin et al., 1993; Reinicke et al., 2010), there are fewer that have combined these two elements into a single experimental procedure (e.g. Fredd et al., 2001; Guo et al., 2013; Zhang et al., 2015). There are also few studies investigating low porosity or ‘tight’ sandstone, compared to (say) shale. This is important as the hydraulic properties of low porosity rocks is significantly modified by both pressure and the presence of larger macro-fracture (Nara et al., 2011), and are often highly anisotropic due to small scale crossbedding, such as in COS (e.g. Gehne and Benson, 2019).

Here, we have focused on hydraulic fracture in tight sandstone with fluid flow measurement directly after this stage in order to assess fluid flow as a function of anisotropy across cycles of confining pressure. This coupled process is particularly important when considering cyclical extraction of fluids that, in turn, changes the effective pressure, such as in the charge/re-charge cycles of geothermal extraction or unconventional hydrocarbon extraction. In our experiments, we find an interplay between the inherent anisotropy of the fracturing materials, with samples cored with long axis perpendicular having a higher breakdown pressure than those parallel to bedding. In all cases, and irrespective of bedding, the cycles of effective pressure have a largely irreversible effect on fluid flow, and with a larger proportionate decrease than in rocks without a fracture network (Gehne and Benson, 2017). This is consistent with past studies, including from large sample volumes (Guo et al., 2013; Tan et al., 2018). Hence, a better understanding of micro-scale fracture is likely to be helpful in optimizing larger scale hydraulic fracture design if the effects of both anisotropy and burial pressure (as a proxy for burial depth) may be incorporated.

FIGURE 13

FIGURE 14

Effect of Anisotropy

Results from the mechanical data, backed up by AE data, show that bedding plane orientation has a pronounced effect on the strength and energy release during tensile fracture. However, these effects are more pronounced at low confining pressure (5 MPa) where we measure a breakdown pressure of 11 MPa (parallel) and 15 MPa (perpendicular) (Fig. 4 & 5) and (Fig. 5). However, this effect rapidly decreases with increasing confining pressure. In every case, breakdown is accompanied by a significant swarm in AE output, and for 5 MPa and 11 MPa confining pressures, with higher cumulative AE counts in experiments conducted perpendicular to bedding compared to parallel to bedding, suggesting these orientations release more energy. However, this pattern is not seen in the data from 16 MPa (Fig. 8 and Fig. 9) suggesting a higher tensile strength in rocks when the tensile stress is normal to bedding due to a more complex fracture morphology, where the tensile fracture must cut through the rock bedding planes (Gehne and Benson, 2019; Hu et al., 2017).

In addition to the cumulative AE counts, more pre-facture acoustic events are recorded in data at 5 MPa (Fig 4 and Fig. 5) and in data parallel to bedding at 11 MPa (Fig. 6). We attribute this effect to the lower effective pressure in these experiments promoting earlier fracture nucleation compared to data from experiment perpendicular to bedding (Fig. 7) compared to the data from the highest confining pressure of 16 MPa (Fig. 8 and 9) that suppress early hydrofracture events. This is supported by fact that no AE data is recorded before 4955s and 6918s (Fig. 8 and 9 respectively).

Anisotropy provides the major influence on fluid flow, with samples cored parallel to the bedding orientation recording a high fluid flow rate at a given confining pressure when compared to the experiments with sample cored perpendicular to the bedding orientation. Our data reveal an initial fluid flow anisotropy (the ratio of flow in samples fractured perpendicular to parallel to bedding) of 0.4 at 5 MPa, 0.9 at 11 MPa, and 0.3 at 16 MPa, illustrating a very low fluid flow anisotropy even at high effective pressures. This general result is consistent with that obtained by Gehne and Benson (2017), which shows that fluid flow is significantly influenced by bedding plane orientation. However, the fluid flow anisotropy as measured on our tensile fracture samples is generally lower than the equivalent permeability anisotropy measured in unfractured samples (Benson et al., 2005; Gehne, and Benson 2017) particularly at high effective pressures. Our data compares to fluid flow (permeability) anisotropy of 16.5-25% as reported for unfractured Crab Orchard sandstone at 5-30 MPa confining pressure (Gehne and Benson, 2017).

To better understand the complexities of heterogeneity and fluid flow, we have collected X-Ray Computed Tomography (XCT) data on each sample post-test (Figure 13). These images were then segmented in Avizio to extract an approximate tensile fracture tortuosity with bedding plane orientation (Fig. 14). Using this, we note that samples cored parallel to bedding exhibit a slightly lower fracture thickness of about 35 microns (COSx-1; Fig. 14A), while samples cored perpendicular to bedding have fracture thickness of about 45 microns (COSz-1; Fig. 14B). However, we also note that the fluid flow data, both pre- and -post fracture, is likely to follow a largely radial pathway, whereas the comparison to Gehne and Benson (2017) is to a linear Darcy flow along the cylindrical sample. Hence, we present fluid flow in this study rather than permeability. Also, our data suggests that the fracture geometry is influenced by the bedding orientation (anisotropy) during injection. Whereas a single fracture tends to develop in samples cored parallel and perpendicular to bedding at a low confining pressure (5MPa), at elevated confining pressure (11MPa and 16MPa), two fractures tend to be formed (Figure 13).

Effect of Confining Pressure

The increase of initial confining pressure from 5 MPa, through 11 MPa, and to 16 MPa has the overall effect of increasing the breakdown pressure respectively to 10, 27, and 40 MPa for samples parallel to bedding, and to 15, 26, and 35 MPa perpendicular to bedding. This is consistent with the findings of Jaeger et al. (2009) and Haimson and Fairhurst (1969) who postulated that an increase in confining pressure increases the horizontal stresses and hence a resultant increase in breakdown pressure as expressed in equation(s) 1-4. A key output when considering fluid flow thought newly generated tensile fracture is the pressure history on fracture properties (a key control on the bulk fluid flow).

Previous data focusing on cyclical fluid flow on solid samples of COS have reported a reduction of permeability in subsequent cycles of between approximately 66% to 70% (Gehne & Benson, 2017). For fluid flow through a tensile fracture, as shown here, the equivalent decrease per fluid flow cycles ranges from 92% (COSx-3) to 68% (COSx-2) to 95% (COSx-1). This suggests that the addition of the tensile fracture increases the compliance of the rock, and therefore makes the application of confining pressure more sensitive when measured in terms fluid flow. Similar effects were also reported by Nara et al. (2011).

We also find that the hysteresis in fluid flow is more sensitive to the overall specimen anisotropy (i.e. whether fluid flow is parallel to perpendicular to bedding) rather than the XCT-measured fracture thickness. At each initial pressure, post fracture flow rate is lower in the z-orientation samples (Fig. 1) compared to x-orientation despite larger fracture aperture (Fig. 14). This suggests that these larger average apertures are generally more tortuous, resulting in a lower flow rate, which is consistent with fracture in the z-orientation, or so-called divider orientation, where the tensile fracture crosses multiple layers of bedding (Gehne et al., 2020).

As the elevated confining pressure is released and restored to its initial state at injection, the fluid flow does tend to recover, but not to its initial value at injection. This phenomenon is known as flow hysteresis and has been widely studied and reported (e.g. Gehne and Benson 2017). It is also likely that rocks with significant clay and fine crossbedding, such as this tight sandstone, results in tensile fractures of low compliance, and therefore causing them to fail to reopen during subsequent pressure cycles. This would also be manifested as an irreversible decrease in the fracture aperture and therefore lower permeability (Walsh, 1981; Vinciguerra et al., 2014).

Conclusions

In this study we have investigated the influence of confining pressure and anisotropy on fluid flow through tensile fracture under simulated in-situ pressures relevant to hydraulic fracture in a low porosity (tight) sandstone (Crab Orchard). We find that a general increase trend in breakdown pressure and cumulative acoustic emission when confining pressure increases, which leads to an irreversible decrease in fluid flow through the tensile fracture when confining pressure is cycled. In addition, breakdown pressure is higher in experiments with samples cored parallel to bedding at a lower confining pressure (5MPa), this effect decreases at higher confining pressure (11MPa and 16MPa) at injection. We conclude that anisotropy is a significant contributing factor to both the fluid flow hysteresis effect and breakdown stress, with the tortuosity a key factor rather than fracture aperture alone in describing fluid flow rate through the fracture.

In general, the fluid flow is higher in experiments with samples cored parallel to bedding and additionally has weaker recoverability when confining pressure is ‘re-set’. We observed two stages of flow rate reduction during in the two cycles of confining pressure. The first cycle of confining pressure is identified by a rapid decrease in flow rate (e.g. 97% for COSx-1 and 95% for COSz-1) while the second cycle is characterized by a slow decrease in flow rate (e.g. 79% for COSx-1 and 86% for COSz-1). We conclude that it is likely that a combination of mechanisms operate, and must be considered in determining the overall permeability of tight sandstone to regional stresses during burial and upliftment (expressed as confining pressure cycles and 're-set'). This is not limited to tight sandstone but also a low permeability anisotropic rock material such as shale and mudstone. Finally, we suggest that the open fracture compliance is also important, particularly with regards to cyclical pressure and stress, which is further complicated for rocks such as Crab Orchard that have significant clay content.

References

Benson, P., Schubnel, A., Vinciguerra, S., Trovato, C., Meredith, P. and Young, R.P., 2006. Modeling the permeability evolution of microcracked rocks from elastic wave velocity inversion at elevated isostatic pressure. Journal of Geophysical Research: Solid Earth, 111(B4).

Benson, P.M., Meredith, P.G. and Platzman, E.S., 2003. Relating pore fabric geometry to acoustic and permeability anisotropy in Crab Orchard Sandstone: A laboratory study using magnetic ferrofluid. *Geophysical research letters*, *30*(19).

Benson, P.M., Meredith, P.G., Platzman, E.S. and White, R.E., 2005. Pore fabric shape anisotropy in porous sandstones and its relation to elastic wave velocity and permeability anisotropy under hydrostatic pressure. *International Journal of Rock Mechanics and Mining Sciences*, *42*(7-8), pp.890-899.

Bernier, F. and Bastiaens, W., 2004. Fracturation and self-healing processes in clays–The SELFRAC Project. *Proceedings of EURADWASTE*, *4*, pp.478-491.

Fazio, M., Ibemesi, P., Benson, P., Bedoya-González, D. and Sauter, M., 2021. The Role of Rock Matrix Permeability in Controlling Hydraulic Fracturing in Sandstones. *Rock Mechanics and Rock Engineering*, pp.1-26.

Fredd, C.N., McConnell, S.B., Boney, C.L. and England, K.W., 2001. Experimental study of fracture conductivity for water-fracturing and conventional fracturing applications. *SPE journal*, *6*(03), pp.288-298.

Gehne, S. and Benson, P.M., 2017. Permeability and permeability anisotropy in Crab Orchard sandstone: Experimental insights into spatio-temporal effects. *Tectonophysics*, *712*, pp.589-599.

Gehne, S. and Benson, P.M., 2019. Permeability enhancement through hydraulic fracturing: laboratory measurements combining a 3D printed jacket and pore fluid over-pressure. *Scientific reports*, *9*(1), pp.1-11.

Gehne, S., 2018. *A laboratory study of fluid-driven tensile fracturing in anisotropic rocks* (Doctoral dissertation, University of Portsmouth).

Gehne, S., Forbes Inskip, N.D., Benson, P.M., Meredith, P.G. and Koor, N., 2020. Fluid-driven tensile fracture and fracture toughness in Nash point shale at elevated pressure. *Journal of Geophysical Research: Solid Earth*, *125*(2), p.e2019JB018971.

Gillard, M.R., Medvedev, O.O., Hosein, P.R., Medvedev, A., Peñacorada, F. and d'Huteau, E., 2010, January. A new approach to generating fracture conductivity. In *SPE Annual Technical Conference and Exhibition*. Society of Petroleum Engineers.

Guo, T., Zhang, S., Gao, J., Zhang, J. and Yu, H., 2013. Experimental study of fracture permeability for stimulated reservoir volume (SRV) in shale formation. *Transport in porous media*, *98*(3), pp.525-542.

Haimson, B. and Fairhurst, C., 1969, January. In-situ stress determination at great depth by means of hydraulic fracturing. In *The 11th US symposium on rock mechanics (USRMS)*. American Rock Mechanics Association.

Hu, S.C., Tan, Y.L., Zhou, H., Guo, W.Y., Hu, D.W., Meng, F.Z. and Liu, Z.G., 2017. Impact of bedding planes on mechanical properties of sandstone. *Rock Mechanics and Rock Engineering*, *50*(8), pp.2243-2251.

Hubbert, M.K. and Willis, D.G., 1972. Mechanics of hydraulic fracturing.

Jaeger, J.C., Cook, N.G. and Zimmerman, R., 2009. *Fundamentals of rock mechanics*. John Wiley & Sons.

Kennedy, R.L., Knecht, W.N. and Georgi, D.T., 2012, January. Comparisons and contrasts of shale gas and tight gas developments, North American experience and trends. In *SPE Saudi Arabia Section Technical Symposium and Exhibition*. Society of Petroleum Engineers.

Kranz, R., Frankel, A., Engelder, T. and Scholz, C. (1979). The permeability of whole and jointed Barre granite. In: International Journal of Rock Mechanics and Mining Sciences & Geomechanics Abstracts, 16 (4), 1979, p.225–234.

Ma, L., Taylor, K.G., Lee, P.D., Dobson, K.J., Dowey, P.J. and Courtois, L., 2016. Novel 3D centimetre-to nano-scale quantification of an organic-rich mudstone: The Carboniferous Bowland Shale, Northern England. *Marine and Petroleum Geology*, *72*, pp.193-205.

Martin, C.D. and Chandler, N.A., 1993, December. Stress heterogeneity and geological structures. In *International journal of rock mechanics and mining sciences & geomechanics abstracts* (Vol. 30, No. 7, pp. 993-999). Pergamon.

Nara, Y., Meredith, P.G., Yoneda, T., Kaneko, K., 2011. Influence of macro-fractures and micro-fractures on permeability and elastic wave velocities in basalt at elevated pressure. Tectonophysics 503, 52-59.

Reinicke, A., Rybacki, E., Stanchits, S., Huenges, E. and Dresen, G., 2010. Hydraulic fracturing stimulation techniques and formation damage mechanisms—Implications from laboratory testing of tight sandstone–proppant systems. *Geochemistry*, *70*, pp.107-117.

Richards, J.P., 2003. Tectono-magmatic precursors for porphyry Cu-(Mo-Au) deposit formation. *Economic geology*, *98*(8), pp.1515-1533.

Rubin, A.M., 1993. Tensile fracture of rock at high confining pressure: implications for dike propagation. *Journal of Geophysical Research: Solid Earth*, *98*(B9), pp.15919-15935.

Sone, H. and Zoback, M.D., 2013. Mechanical properties of shale-gas reservoir rocks—Part 1: Static and dynamic elastic properties and anisotropy. *Geophysics*, *78*(5), pp.D381-D392.

Stanchits, S., Surdi, A., Gathogo, P., Edelman, E. and Suarez-Rivera, R., 2014. Onset of hydraulic fracture initiation monitored by acoustic emission and volumetric deformation measurements. Rock mechanics and rock engineering, 47(5), pp.1521-1532.

Tan, Y., Pan, Z., Liu, J., Feng, X.T. and Connell, L.D., 2018. Laboratory study of proppant on shale fracture permeability and compressibility. *Fuel*, *222*, pp.83-97.

Teufel, L.W. and Clark, J.A., 1981. *Hydraulic-fracture propagation in layered rock: experimental studies of fracture containment* (No. SAND-80-2219C; CONF-810518-7). Sandia National Labs. Albuquerque, NM (USA).

Tuffen, H. and Dingwell, D., 2005. Fault textures in volcanic conduits: evidence for seismic trigger mechanisms during silicic eruptions. *Bulletin of Volcanology*, *67*(4), pp.370-387

Ulusay, R. ed., 2014. *The ISRM suggested methods for rock characterization, testing and monitoring: 2007-2014*. Springer.

Vinciguerra, S., Meredith, P.G. and Hazzard, J., 2004. Experimental and modeling study of fluid pressure-driven fractures in Darley Dale sandstone. *Geophysical research letters*, *31*(9).

Walsh, J.B., 1981, October. Effect of pore pressure and confining pressure on fracture permeability. In *International Journal of Rock Mechanics and Mining Sciences & Geomechanics Abstracts* (Vol. 18, No. 5, pp. 429-435). Pergamon.

Wang, Q., Chen, X., Jha, A.N. and Rogers, H., 2014. Natural gas from shale formation–the evolution, evidences and challenges of shale gas revolution in United States. *Renewable and Sustainable Energy Reviews*, *30*, pp.1-28.

Zhang, J., Kamenov, A., Zhu, D. and Hill, A.D., 2015. Development of new testing procedures to measure propped fracture conductivity considering water damage in clay-rich shale reservoirs: An example of the Barnett Shale. *Journal of Petroleum Science and Engineering*, *135*, pp.352-359.

Zhang, J., Kamenov, A., Zhu, D. and Hill, A.D., 2015. Measurement of realistic fracture conductivity in the Barnett shale. *Journal of Unconventional Oil and Gas Resources*, *11*, pp.44-52.

Zoback, M.D., Rummel, F., Jung, R. and Raleigh, C.B., 1977, March. Laboratory hydraulic fracturing experiments in intact and pre-fractured rock. In *International Journal of Rock Mechanics and Mining Sciences & Geomechanics Abstracts* (Vol. 14, No. 2, pp. 49-58). Pergamon.

Sample	Length (mm)	Diameter (mm)	Orientation	Pc (MPa)	Pre HF flow rate (mL/min)	Post HF flowrate (mL/mL)	Pb (MPa)
COSx_1	92.34	36.11	Parallel	5	0.036	1.67	11.29
COSz_1	92.15	36.10	Perpendicular	5	0.012	0.6	15.41
COSx_2	94.54	36.10	Parallel	11	0.012	0.043	27.70
COSz_2	90.71	36.12	Perpendicular	11	0.018	0.037	27.30
COSx_3	90.87	36.10	Parallel	16	0.024	0.l27	40.47
COSz_3	90.24	36.10	Perpendicular	16	0.006	0.09	34.24

Table 1: Summary of experimental conditions and sample orientations / dimensions, Pc is confining pressure, Pb is breakdown pressure (the fluid pressure at the moment of tensile fracture), Pre HF (Hydraulic fracture) flow rate and Post HF (Hydraulic fracture) flow rate

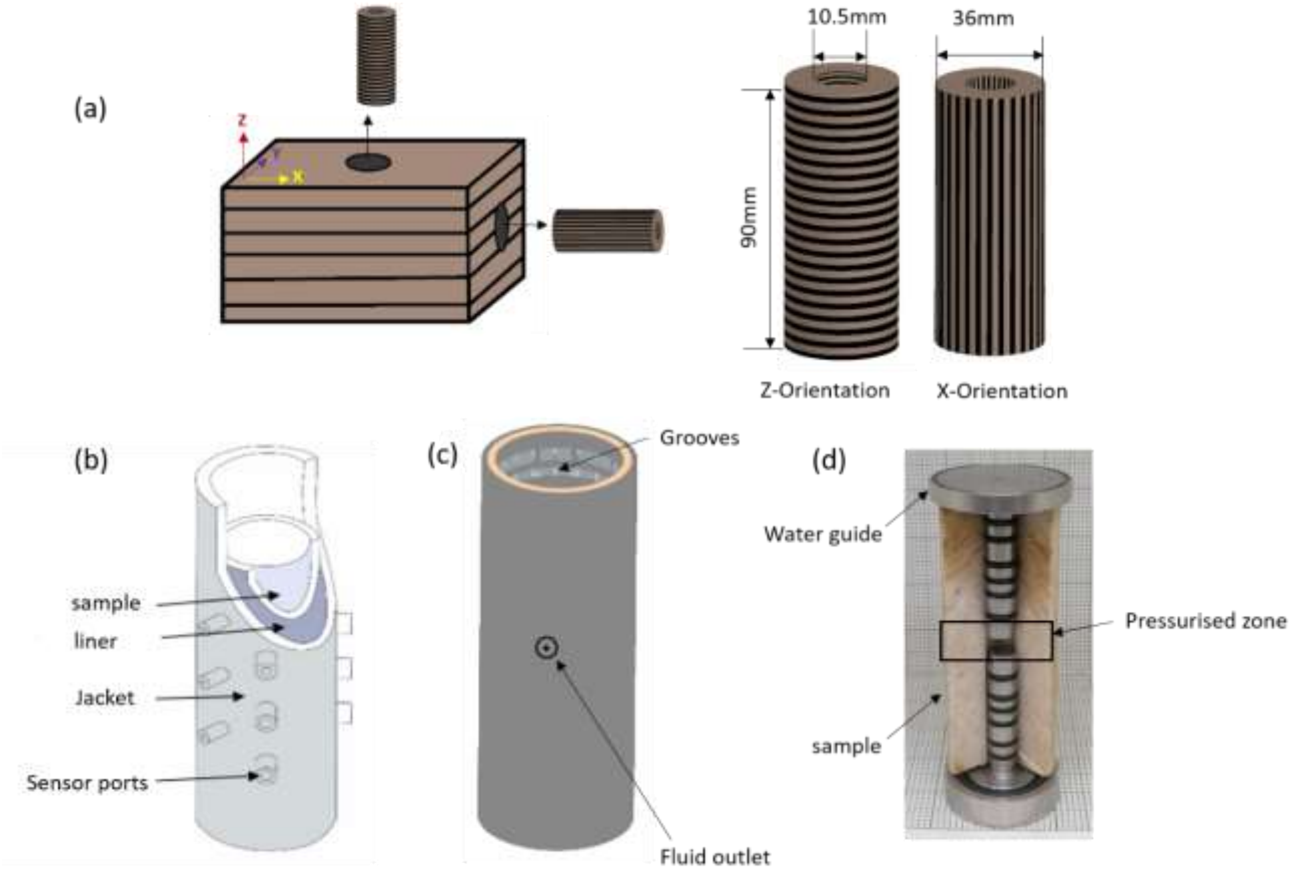

Fig. 1 (a): Sample cored in Z and X orientations with respect to the visible mm-scale crossbedded sandstone. (b): Sample assembled in the liner and rubber jacket. (c): 3D printed water transport liner. (d): Cross section of sample with water guide showing the pressurized zone (modified after Gehne and Benson, 2019)

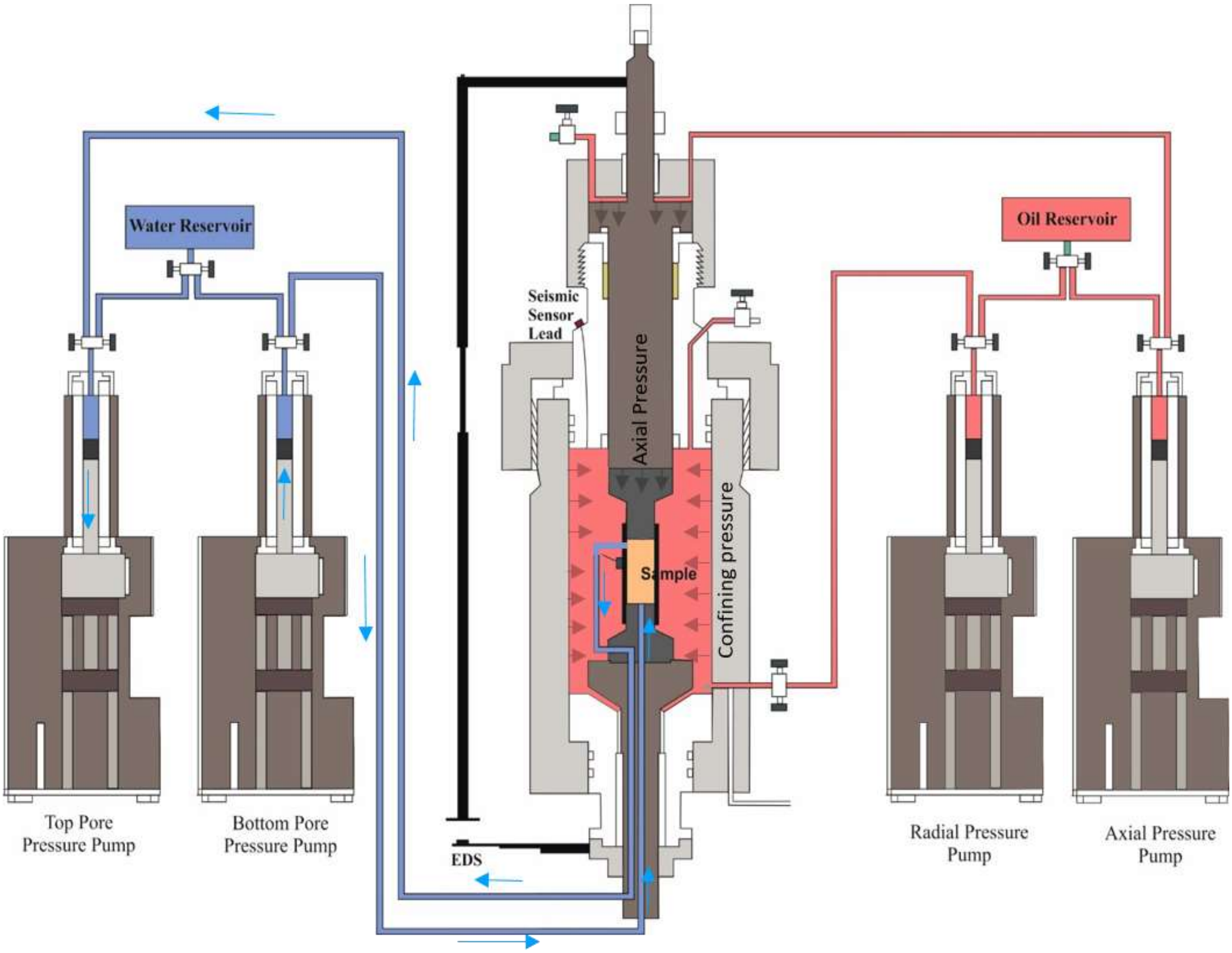

Fig. 2 Schematic of the triaxial apparatus and pump systems

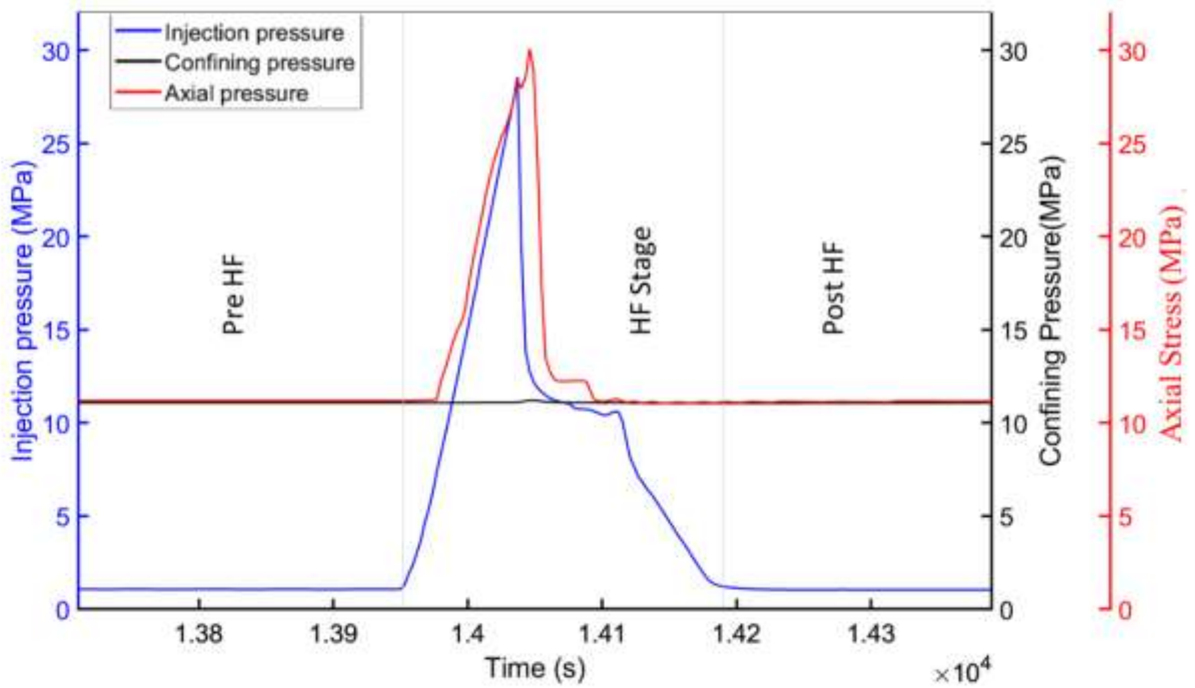

Fig 3 Overview plot of a typical experiment with injection pressure (blue), confining pressure (black) and axial stress (red) with time, showing the 3 experiment stages: (i) Pre-hydraulic fracture (pre HF) flow (after hydrostatic conditions are established); (ii) The hydraulic fracturing stage (HF): axial stress (σ_{ax}) is increased simultaneously with the injection (pore) pressure increase to maintain approximate hydrostatic conditions during fluid injection; (iii) Post hydraulic fracture (Post HF) flow (with hydrostatic conditions re-established)

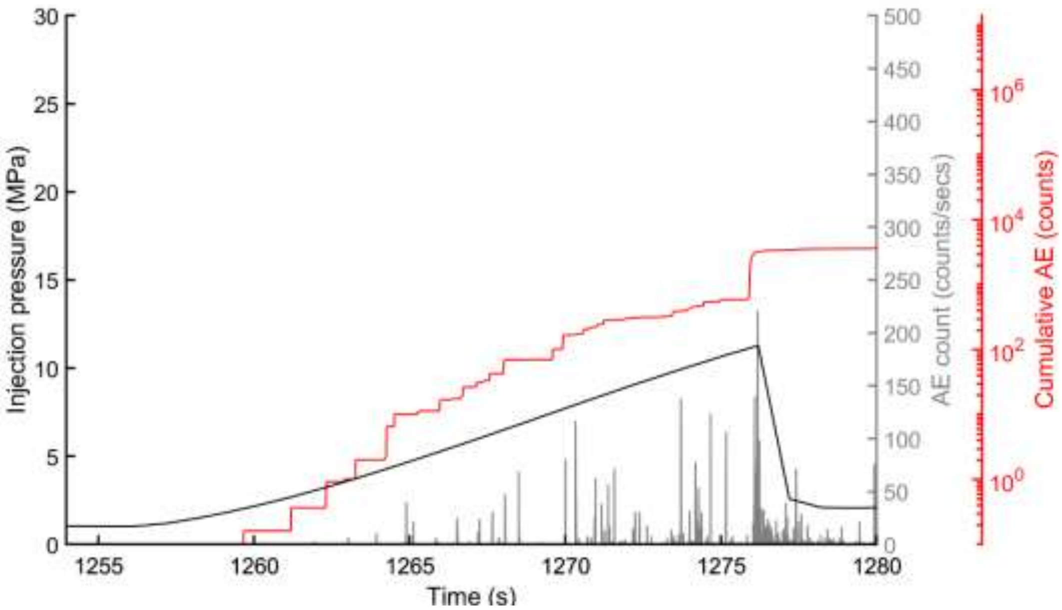

Fig. 4 Mechanical properties and AE in COS during injection at 5MPa initial conditions. Injection pressure (grey continuous line) cumulative AEs (red line) and hit count (grey bar) for sample COSx-1 (parallel to bedding)

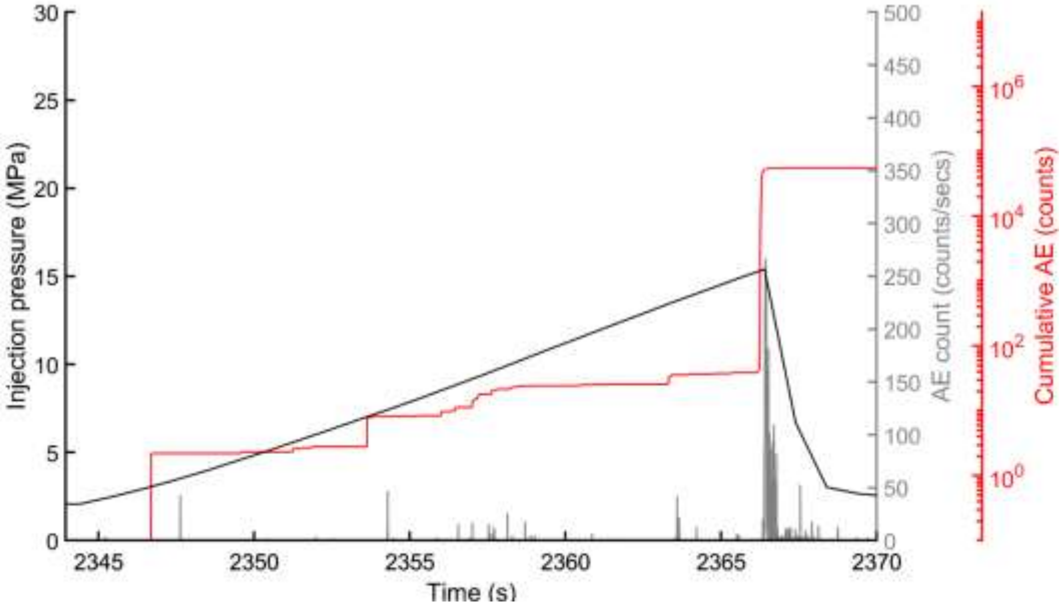

Fig. 5 Mechanical properties and AE in COS during injection at 5MPa initial conditions. Data shown here are the injection pressure (black continuous line), cumulative AEs (red line) and hit count (grey bar) for sample COSz-1 (perpendicular to bedding)

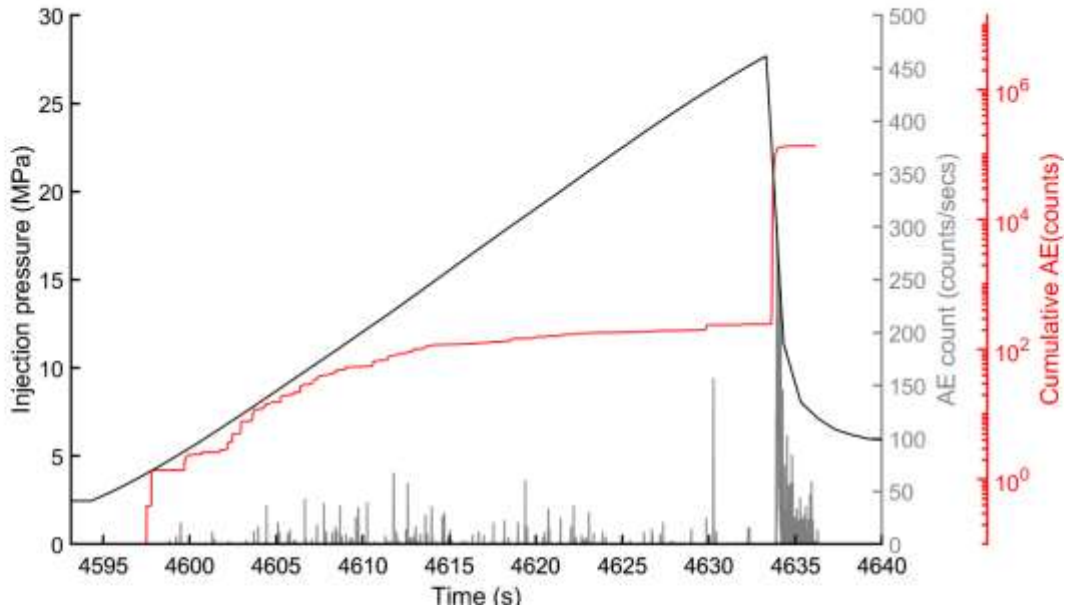

Fig. 6 Mechanical properties and AE in COS during injection at 11MPa initial conditions. Data shown here are the injection pressure (black continuous line), cumulative AEs (red line) and hit count (grey bar) for sample COSx-2(parallel to bedding)

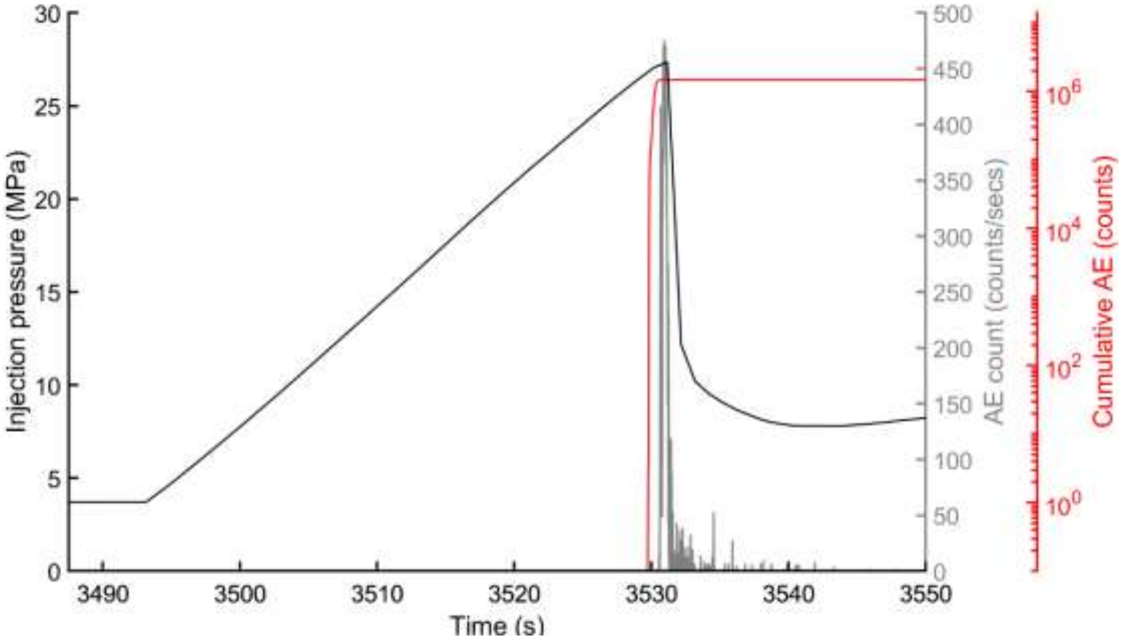

Fig.7 Mechanical properties and AE in sample COSz-2 during injection at 11MPa initial conditions. Injection pressure (black continuous line), injected volume (blue line), cumulative AEs (red line) and hit count (grey bar)

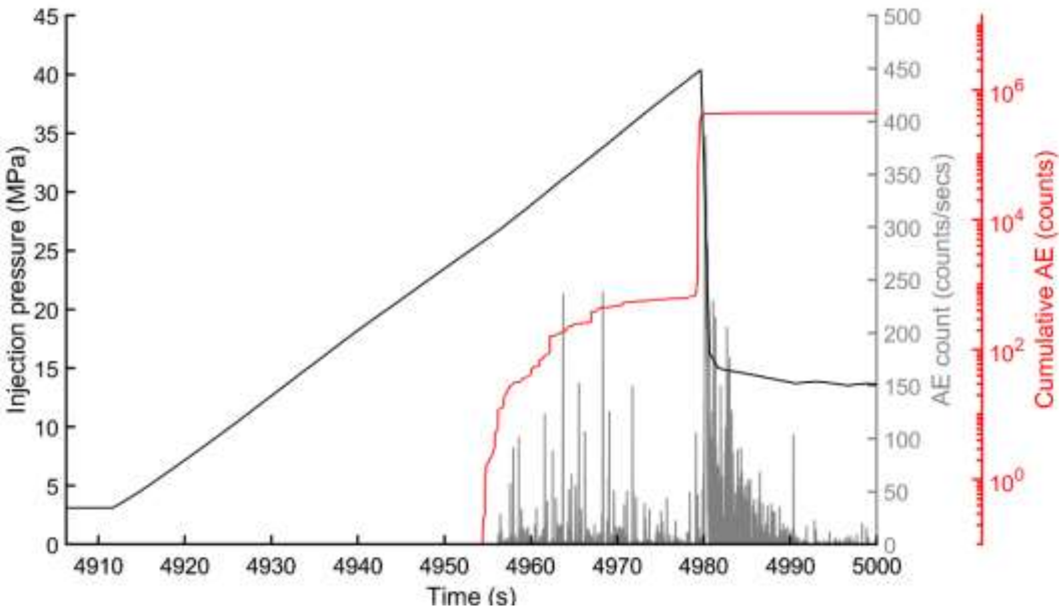

Fig. 8 mechanical property behavior and AE in COS during injection at 16MPa initial conditions. Injection pressure (black continuous line), injected volume (blue line), cumulative AEs (red line) and hit count (grey bar) for sample COSx-3

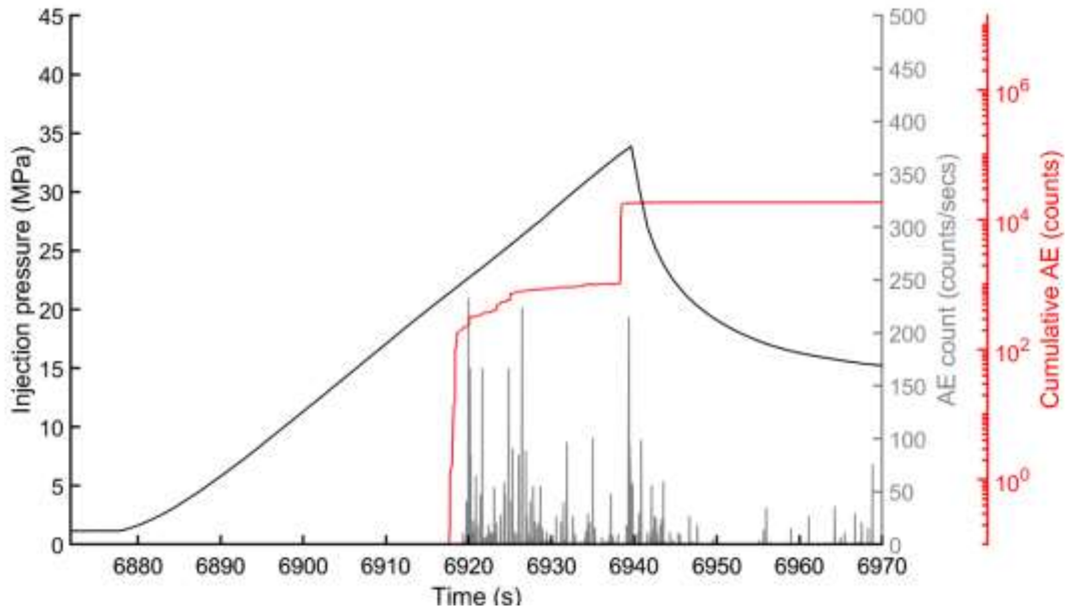

Fig. 9 mechanical property behavior and AE in COS during injection at 16MPa initial conditions. Injection pressure (black continuous line), injected volume (blue line), cumulative AEs (red line) and hit count (grey bar) for sample COSz-3

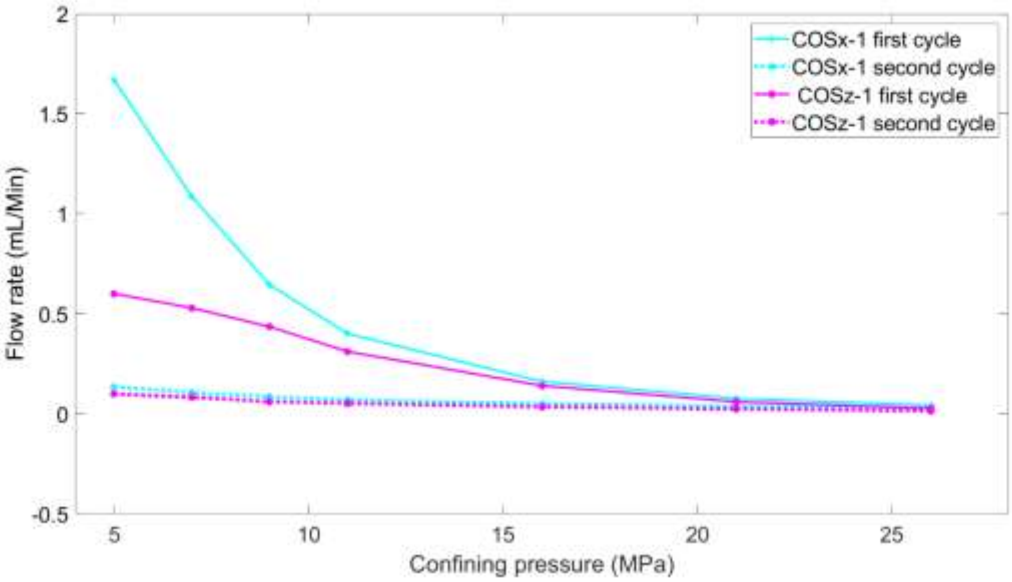

Fig. 10 Average flow rate for first cycle (continuous cyan line) and average flow rate for second cycle (discontinuous cyan line) for COSx-1 and average flow rate for first cycle (continuous pink line) and average flow rate for second cycle (discontinuous pink line) for COSz-1 are calculated at each steady state condition for every confining pressure step, plotted as a confining pressure

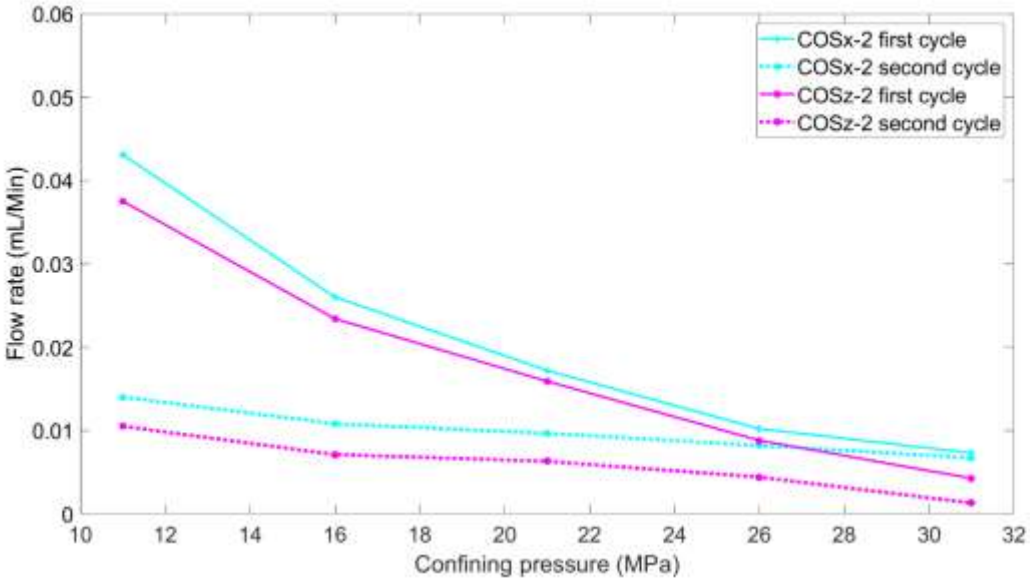

Fig. 11 Average flow rate for first cycle (continuous cyan line) and average flow rate for second cycle (discontinuous cyan line) for COSx-2 and average flow rate for first cycle (continuous pink line) and average flow rate for second cycle (discontinuous pink line) for COSz-2 are calculated at each steady state condition for every confining pressure step, plotted as a confining pressure

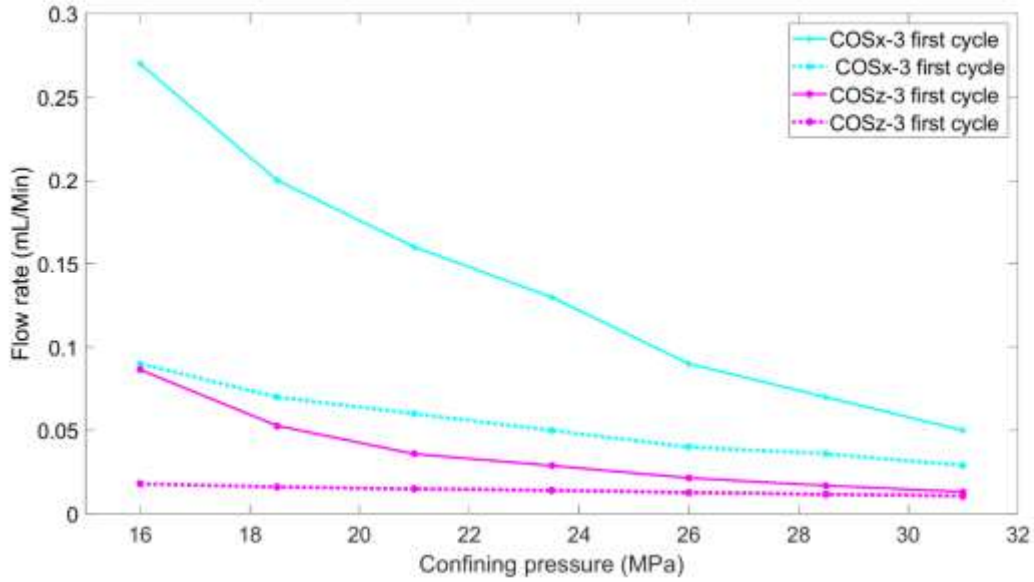

Fig. 12 Average flow rate for first cycle (continuous cyan line) and average flow rate for second cycle (discontinuous cyan line) for COSx-3 and average flow rate for first cycle (continuous pink line) and average flow rate for second cycle (discontinuous pink line) for COSz-3 are calculated at each steady state condition for every confining pressure step, plotted as a confining pressure

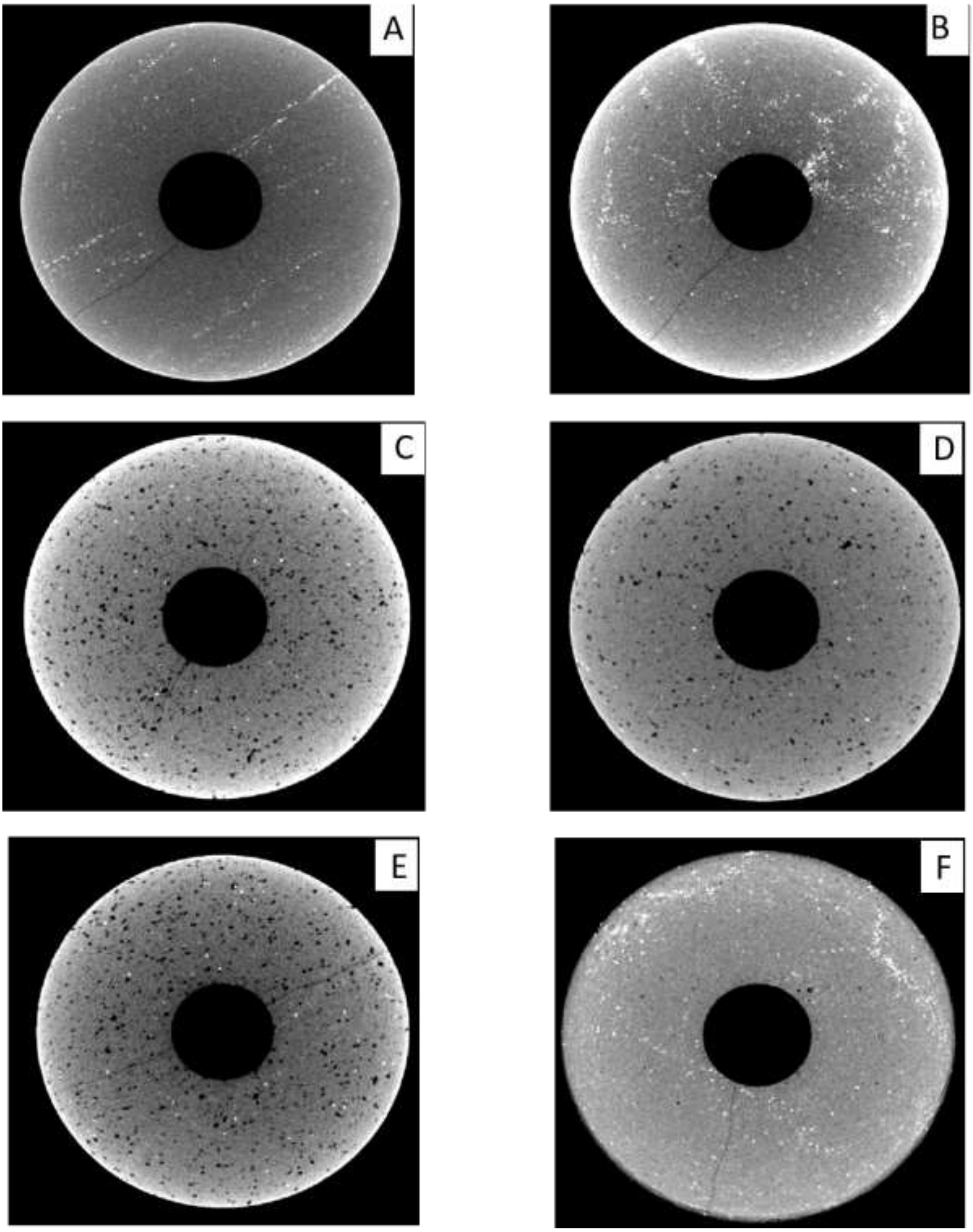

Fig. 13 X-ray Computed Tomography showing tensile fracture: (A) fracture pattern in COSx_1 (B) fracture geometry in COSz_1 (C) fracture pattern in COSx_2 (D) tensile fracture development in COSz_2 (E) tensile fracture pattern in COSx_3 (F) fracture geometry in COSz_3. In all cases a prominent fracture is seen orientated lower-left to top-right, and favoring two fractures in samples cored in the 'x' direction (panels A, C, E) and one in samples cored in the 'z' direction (panels B, D, F)

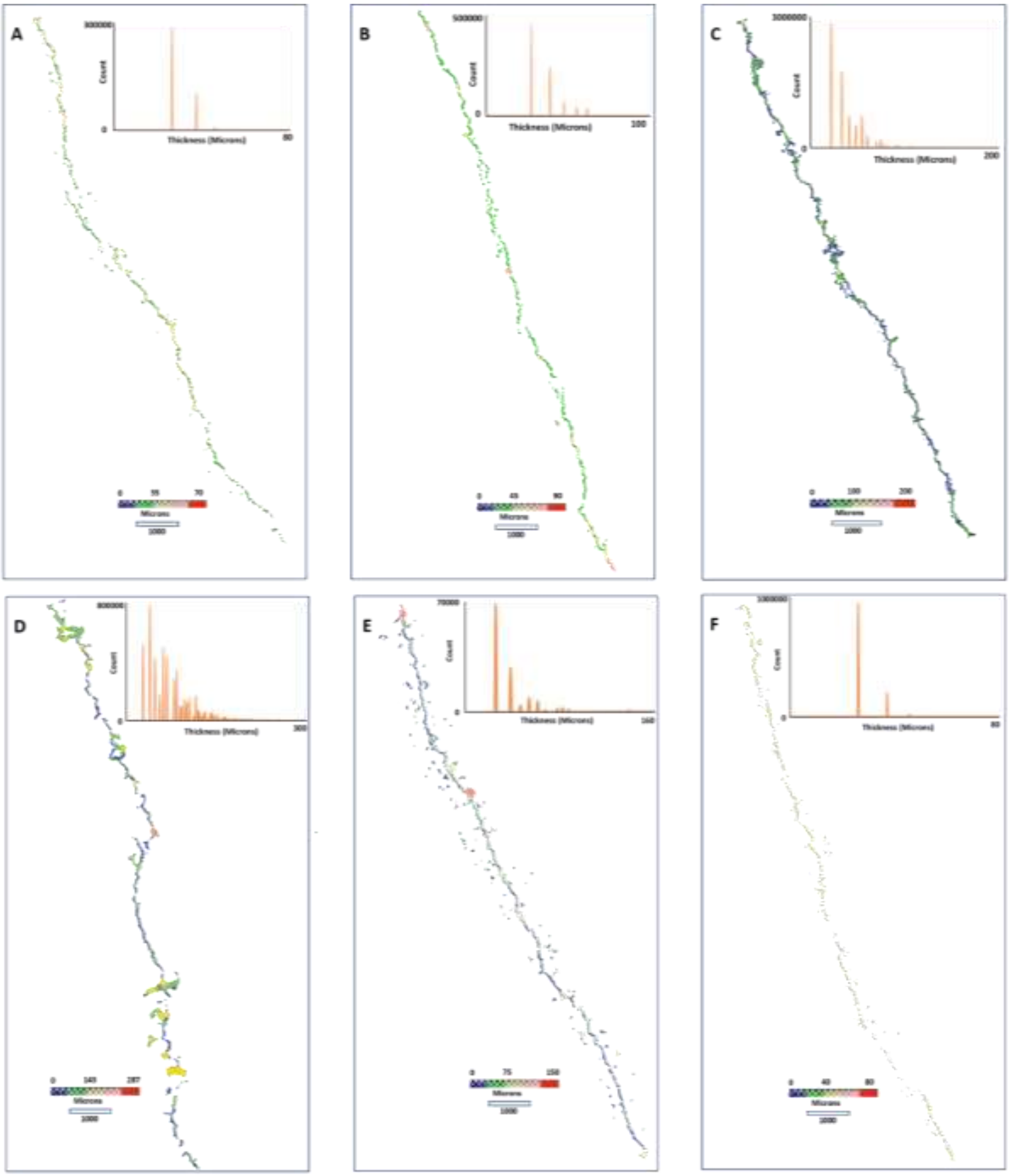

Fig. 14 Analysis of the tensile fracture showing thickness and pore connectivity; The insert is a histogram distribution of the thickness for both fracture and pore space: (A) fracture thickness in COSx-1, average 35 μm (B) fracture geometry in COSz-1, average 45 μm (C) fracture thickness distribution in COSx-2, average 100 μm (D) tensile fracture analysis for COSz-2, average 145 μm (E) tensile fracture thickness in COSx-3, average 75 μm (F) fracture geometry in COSz-3, average 40 μm